Available online at www.sciencedirect.com

ScienceDirect

Journal of Magnesium and Alloys 10 (2022) 2173–2184

www.elsevier.com/locate/jma

Full Length Article

Towards high degree of *c*-axis orientation in MgB_2 bulks

M.A. Grigoroscuta[a], G.V. Aldica[a], M. Burdusel[a], V. Sandu[a], A. Kuncser[a], I. Pasuk[a], A.M. Ionescu[a], T.S. Suzuki[b], O. Vasylkiv[b], P. Badica[a,*]

[a] *National Institute of Materials Physics, 405A Street Atomistilor, Magurele 077125, Romania*
[b] *National Institute for Materials Science, 1-2-1 Sengen, Ibaraki, Tsukuba 305-0047, Japan*

Received 19 June 2021; received in revised form 1 September 2021; accepted 10 October 2021
Available online 7 December 2021

Abstract

The paper presents fabrication and characterization of spark plasma sintered textured (001) MgB_2 with a record degree of orientation of about 40% and 16% by high-energy ultra-sonication and slip casting in high magnetic field (12 T) and 0 T magnetic field, respectively. Structural characterization was performed by X-ray diffraction, and electron microscopy. The analysis revealed unexpected preferred orientation also in the MgO secondary phase due to the epitaxial growth of (111) MgO on (001) MgB_2. The influence of oriented microstructure on the superconducting characteristics expressed by critical current density (J_c), irreversibility field (H_{irr}), and on the pinning properties were assessed. High anisotropy versus sample orientation in applied magnetic field, H, was observed for J_c, H_{irr}, pinning activation energy (U^*) extracted from relaxation measurements. The zero-field critical current, J_{c0} and $F_{p,max}$ are weakly or not dependent on the direction of H, while the other indicated parameters are significantly influenced. Results enable control of superconducting parameters by further optimization of microstructure through MgB_2 texturing as a novel and viable strategy for development of bulk MgB_2 with enhanced properties when taking advantage of its anisotropy.

Keywords: Textured MgB_2 bulk; Slip casting; Spark plasma sintering; Critical current density; Pinning force; Pinning activation energy.

1. Introduction

MgB_2 occupies a special niche among practical superconductors. It has a convenient critical temperature T_c of 39 K, about two times higher than for the low temperature metallic superconductors (e.g. 18 K for Nb_3Sn). Therefore, this enables the use of MgB_2 in the temperature range of 15–30 K. Liquid hydrogen (20 K) can be used as a cooling agent and technologies based on it are recognized to show enormous potential for development of the future green economy. MgB_2 is a lightweight material. Its bulk density of 2.63 g/cm^3 is a few times lower than for other practical superconductors including high temperature superconductors (e.g. 6.3 g/cm^3 for $YBa_2Cu_3O_7$). Hence, MgB_2 is a valuable superconductor especially for portable applications, in space, transportation, medicine, energy and others. However, to take advantage of the presented features, the improvement of the critical current density, J_c, and of the irreversibility field, H_{irr}, is required. Since the coherence length is relatively large in MgB_2, about 10–40 nm [1], introduction of size-comparable defects can promote vortex pinning and enhancement of J_c and H_{irr}. Literature indicates a few routes such as use of additives and of different processing technologies. In the first case, precipitates of secondary phases and defects associated with them (interfaces, strain at interfaces, local non-stoichiometry, modification of the grain boundaries) or direct substitution of a component element into the crystal lattice of MgB_2 (e.g., carbon for boron [2–4]) can generate effective pinning centers. Modification of the microstructure (e.g. nano-structuring for a high density of grain boundaries as pinning centers) and enhancement of the bulk density are induced by specific technological procedures [5–23], popular being high-energy ball milling and pressure-assisted techniques. Heat treatments in

* Corresponding author.
E-mail address: petre.badica@infim.ro (P. Badica).

https://doi.org/10.1016/j.jma.2021.10.013

reactive atmospheres are also effective for pinning centers insertion. Spark plasma sintering in N_2 atmosphere generated nano-precipitates of the MgB_9N phase enhancing the critical current density at high magnetic fields [24].

A novel strategy is to obtain (001) textured MgB_2 bulks with enhanced transport properties for a preferential direction [19,25]. Samples were fabricated by magnetic field slip casting (MFSP) followed by spark plasma sintering (SPS). Textured powder-in-tube tapes obtained by mechanical deformation and annealing were also reported [26,27]. The MgB_2 has a hexagonal, anisotropic crystal structure with (*ab*)-planes of boron and Mg stacked in the *c*-axis direction. Despite the feeble magnetic properties at room temperature of MgB_2, its anisotropy promotes orientation in MFSP [28,29] which can be further enhanced by spark plasma sintering. In the partially oriented samples with an orientation degree of 21%, J_c and H_{irr} were pushed to higher values in the favorable direction, while in the disadvantageous one, J_c and H_{irr} had a small suppression when compared to a randomly oriented sample [19]. These samples have also shown a complex behavior of the volume pinning force, F_p.

This work reports fabrication and properties of (001) MgB_2 textured bulk samples with a higher degree of orientation than in the previous attempts [19,25]. Orientation enhancement is induced by high-energy ultra-sonication for de-agglomeration and homogenization [30] of the colloidal solution of MgB_2 in ethyl alcohol during slip casting processing. A record orientation degree of about 40% is obtained after spark plasma sintering (SPS) in vacuum or nitrogen if a high magnetic field is applied during slip casting, compared to 16% obtained in zero-field slip casting. The influence of oriented microstructure on superconducting characteristics J_c and H_{irr} and on pinning properties is assessed.

2. Material and methods

Sample processing is presented in Fig. 1. A colloidal solution of powder MgB_2 (99.5% purity, metal basis, LTS Research Laboratories Inc. US) in ethanol was prepared under high energy ultrasound sonication (600 W) (Fig. 1a, b). The as-prepared solution was slip casted (SC) and the resulting compact was spark plasma sintered (SPS) (sample M1, Table 1). Slip casting experiments were also performed under a magnetic field, H_0, of 12 T (Fig. 1c). The as-resulting casted compacts were spark plasma sintered in vacuum (30 Pa) (sample M2, Table 1) or in a N_2 atmosphere (91 kPa) (sample M3, Table 1, Fig. 1d, e). Spark plasma sintering was performed at 1150 °C for 30 min, using a FCT Systeme GmbH—HP D 5 (Germany) sintering furnace, with graphite die systems. The heating rate was 150 °C/min and the maximum uniaxial pressure applied on the disk-shaped samples (20 mm diameter and 3 mm thickness) was 95 MPa. Noteworthy is that different from our previous works [19,25], no dispersing agent was introduced in the colloidal solution. Instead, as already mentioned, the colloidal solution was sonicated at high energy.

XRD patterns were obtained with a Bruker-AXS D8 ADVANCE diffractometer ($Cu_{K\alpha}$ radiation). From Rietveld

Table 1
Samples, apparent (ρ_a^{SPS}) and relative density (R^{SPS}), Lotgering factor *LF*, March Dolase orientation factor *r*, the degree of orientation η, and the orientation angle φ of MgB_2 and MgO, microstrain (ε) in MgB_2 and MgO, phase content. The notations correspond to those in Fig. 2a. *H* is applied magnetic field during magnetic measurements.

Sample	MgB_2 sample type	Apparent density, ρa^{SPS} (g/cm^3) / Relative density, R^{SPS} (%)	Microstrain in MgB_2 ε(%)	Microstrain in MgO	Phase content (wt.%), Crystallite size (nm) and orientation parameters							
					MgB_2			MgO			MgB_4	
					wt.%	nm	*LF* (%) / *r* / η (%)/φ (°) MgB_2 (001)	wt.%	nm	η (%)/φ (°) MgO (111)	wt.%	nm
M0	Raw powder	- / -	0.075 ± 0.005	0.06 ± 0.02	97.0	113 ± 3	0 / - / - / -	1.8	45 ± 4	- / -	Mg (1.2)	–
M1	0 T-SC + SPS- vacuum; S_{top} M1$_{\|\|}$ ($H \parallel H_0$)	2.678 / 100	0.12 ± 0.0004	0.114 ± 0.01	82.3	187 ± 2	12.6 / 0.754 / 16.1 / 49	8.8	177 ± 16	~0 / -	8.9	92 ± 4
	0 T-SC +SPS- vacuum; S_{side} M1$_{\perp}$ ($H \perp H_0$)		0.10 ± 0.0006	0.09 ± 0.01	82.5	265 ± 9	- / - / - / -	8.6	154 ± 16	- / -	8.9	99 ± 4
M2	12 T -SC + SPS- vacuum; S_{top} M2$_{\|\|}$ ($H \parallel H_0$)	2.682 / 100	0.11 ± 0.006	0.132 ± 0.015	81.3	220 ± 5	61.6 / 0.473 / 40.5 / 39.9	10.0	184 ± 27	28.2 / 45	8.7	94 ± 3
	12 T-SC + SPS- vacuum; S_{side} M2$_{\perp}$ ($H \perp H_0$)		0.095 ± 0.001	0.124 ± 0.015	82.1	184 ± 5	- / - / - / -	9.5	164 ± 3	- / -	8.4	85 ± 7
M3	12 T-SC + SPS- nitrogen; S_{top} M3$_{\|\|}$ ($H \parallel H_0$)	2.685 / 99.9	0.11 ± 0.001	0.121 ± 0.012	80.1	203 ± 1	60.4 / 0.482 / 39.6 / 40.2	10.2	187 ± 37	28.2 / 45	9.7	90 ± 8
	12 T-SC + SPS- nitrogen; S_{sid} M3$_{\perp}$ ($H \perp H_0$)		0.095 ± 0.001	0.139 ± 0.013	81.2	174 ± 3	- / - / - / -	9.6	158 ± 25	- / -	9.2	82 ± 7

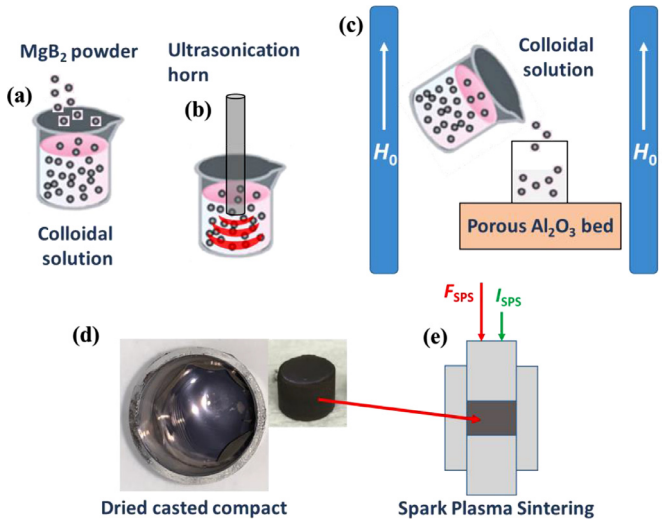

Fig. 1. Processing steps: (a) Colloidal solution preparation; (b) high-energy ultrasonication; (c) slip casting under 12 T; (d) dried casted compact; (e) spark plasma sintering.

analysis (software MAUD 2.31 [31]) the weight fractions and the crystallite size of the detected phases, a and c lattice parameters of MgB_2, and the microstrain for MgB_2 and MgO were determined. In order to obtain a good fit by Rietveld refinement, the preferred orientation of MgB_2 and MgO had to be taken into account, and the March–Dollase orientation parameter r [32], was extracted. We further used this parameter for the calculation of the degree of preferred orientation parameter η, and the characteristic angle φ [33]:

$$\eta = \left[\frac{(1-r)^3}{(1-r^3)}\right]^{1/2} \cdot 100\ (\%) \tag{1}$$

$$\cos\varphi = \left[\frac{1-r}{1-r^3}\right]^{1/2} \tag{2}$$

The degree of preferred orientation η means the excess volume fraction of crystallites having the preferred orientation axis (which is [001] for MgB_2 and [111] for MgO, as shown below) within the surface normal and the angle φ, compared with a random sample. φ is the angle from the surface normal for which the orientation probability in a textured sample equals the orientation probability in a random sample. (For a random sample: $r = 1$, $\eta = 0$, φ is undefined). We expressed the orientation degree of MgB_2 also in terms of the Lotgering factor, LF [34], which is commonly used in the literature.

The apparent densities ρ_a^{SPS} of the SPSed pellets were measured by Archimedes method (in toluene media). The relative densities R^{SPS} (%) were calculated as $R^{SPS} = \rho_a^{SPS}/\rho_t^{SPS} \times 100$. The theoretical densities ρ_t^{SPS} of the composites were determined by the procedure described in Ref. [35]. The phases used in calculation of the theoretical density were MgB_2 (2.63 g/cm^2), MgO (3.58 g/cm^2), and MgB_4 (2.49 g/cm^3).

SEM Lyra3XMU and TEM JEM 2100 microscopes were employed to observe the microstructure of the samples. For SEM, bulk MgB_2 samples were polished and etched for 70 s in Royal water (aqua regia).

Magnetization measurements as a function of the applied field $m(H)$ at different temperatures T and as a function of temperature $m(T)$ at 0.01 T, as well as the relaxation of the magnetization $m(t)$ were performed with a MPMS-SQUID 7T (Quantum Design, US) magnetometer. The samples for magnetic measurements were cut from the center of the sintered disks and have approximately a cuboidal shape ($\sim L \times l \times g = 1.1 \times 1.05 \times 1$ mm^3). To determine the critical current density J_c, the Bean formula for a plate-like geometry [36] was used:

$$J_c = 20 \cdot |m\uparrow - m\downarrow| / \{V \cdot l \cdot [1 - (l/(3 \cdot L))]\} \tag{3}$$

where $m\downarrow$ and $m\uparrow$ are the magnetic moments in emu for ascending and descending magnetic field, respectively, in the $m(H)$ loops, V is the sample volume in cm^3, and L, l, are in cm. Flux jumps were observed in the $m(H)$ loops on the ascending branch (one jump at $\sim$ 1.45 T) at temperatures below 10 K, 5 K and 15 K for samples M1, M2 and M3, respectively. They were not taken in consideration in our analysis. The pinning force is $F_p = \mu_0 H J_c$. To avoid the complications with macro flux jumps and with estimation of $|m\uparrow - m\downarrow|$ in the classic Bean model, the self-field, J_{c0} (in A/cm^2), was estimated from a modified Bean relation, considering the descending branch of the hysteresis loop [37]:

$$J_c = 60 \cdot |m\downarrow| \cdot / (V\ l) \tag{4}$$

The irreversibility field, H_{irr}, is the field for which $J_c = 100$ A/cm^2. The pinning activation energy was determined from relaxation measurements. Samples were zero field cooled to different temperatures, a magnetic field was applied, and the decay of the magnetic moment in time $m(t)$ was recorded for a time window t_w of 50 min. In the range where $\ln(|m|)$ versus $\ln(t)$ is linear, the normalized vortex-creep activation energy is:

$$U^* = -T \cdot \ln(t) / \cdot \ln(|m|) \tag{5}$$

averaged over t_w. [38,39]. For $U^*(T)$ an external field of 3 T was applied and $U^*(H)$ was measured at 10, 15 and 20 K.

3. Results and discussion

3.1. Structure and microstructure of the investigated samples

Two X-ray diffraction patterns were obtained for each bulk sample, one on the surface S_{top} in which case the scattering vector is parallel with the SPS uniaxial pressing force F_{SPS} and the processing magnetic field during slip casting H_0 and the other on S_{side}, with the scattering vector perpendicular to F_{SPS} and H_0 (Fig. 2a). The patterns measured on S_{top} are presented in Fig. 2b. The qualitative analysis shows the presence of the major phase MgB_2, and of MgO and MgB_4 as the secondary phases. To highlight the [001] texturing of MgB_2, the intensities were represented being divided by the intensity of the (101) line, which is the most intense for a randomly oriented sample. Slip casting and SPS decreases the amount

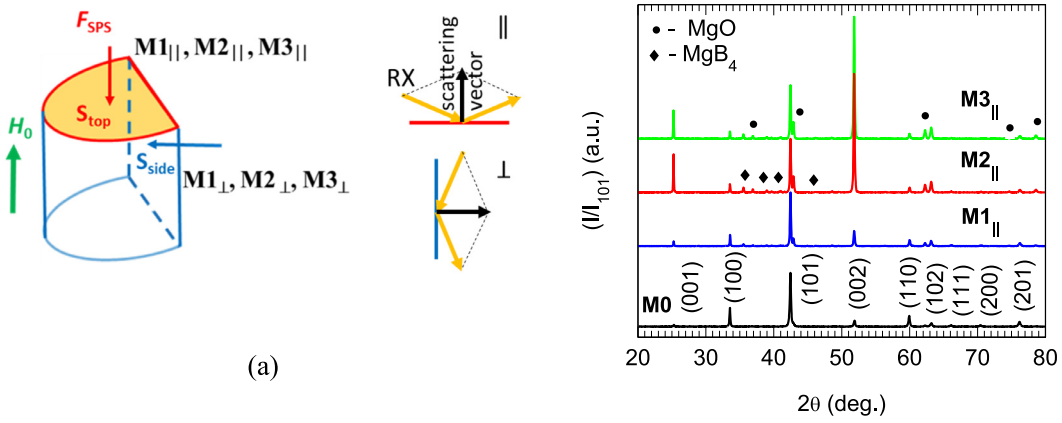

Fig. 2. (a) Notations of the sample surfaces on which the XRD measurements were performed. (b) XRD patterns of the samples obtained on S_{top}.

of MgB_2 (Table 1) from 97 wt.% in the raw powder (sample M0) to 80.1–82.5 wt.% in the sintered bulks (M1, M2, and M3), while the amounts of MgB_4 and MgO increase from 1.8 and 1.2 wt.% to 8.8–10.2 and 8.4–9.7 wt.%, respectively.

Although the amount of the secondary phases is limiting the connectivity within the samples, if properly engineered, these phases can be effective pinning centers [40,41]. Sintered samples show (001) MgB_2 preferred orientation with the (*ab*) plane parallel to S_{top}. A texture with a degree of orientation η of 16.1% ($LF = 12.6\%$) occurs in the sintered sample M1 (Table 1) even in the absence of the magnetic field during slip casting.

We explain this result by the effect of the high energy ultrasonication which breaks the agglomerates of MgB_2 [42]. It is recognized that agglomeration is one of the main limiting factors for mouldability and sintering and cannot be improved in dry powders [43]. The plate-like MgB_2 grains will organize during slip casting in a partially textured green compact and will enhance their texture during subsequent SPS. Enhancement of texture during SPS of a green compact with a low orientation was addressed in an earlier work [19]. For the samples processed by slip casting under a magnetic field of 12 T and SPSed in vacuum or in N_2 atmosphere, a relatively high orientation is achieved with η of 40.5 ($LF = 61.6\%$) and 39.6% ($LF = 60.4\%$), and φ of 39.9 and 40.2°, respectively. Therefore, the preferred orientation of MgB_2 is considerably increased in the samples obtained in a magnetic field.

Another interesting aspect is that for a good Rietveld fitting of the measured XRD patterns of the highly oriented samples M2 and M3, it was necessary to consider a preferred orientation also for MgO, with the (111) plane parallel to S_{top}. In both samples M2 and M3, an excess of about 28% of the MgO crystallites is oriented with the <111> axes within about 45° from the surface normal (direction of H_0). Considering the texturing mode of MgB_2 and MgO, it results that the (111) crystal planes of MgO are oriented preferentially parallel to the (001) plane of MgB_2. The orientation degree of MgO is a bit worse than that of MgB_2 ($\eta = 28\%$ compared to about 40%). A closer look at the atomic structures of the (111) MgO and (001) MgB_2 planes shows excellent theoretical lattice matching that favors the epitaxial growth of MgO on MgB_2 crystallites (Fig. 3d) during SPS. The epitaxial mismatch is (3.0860–2.9797)*100/3.086 = 3.4%. It is expected that the epitaxial stress causes a compression strain in the (*ab*)-plane of MgB_2 at the interface with MgO, and a slight increase of the average MgO lattice parameter. The epitaxial growth of (001) MgB_2 thin films on (111) Si single crystal substrates with a MgO seed layer was reported in Ref. [44]. Fig. 3a and Fig. 3b show an average decrease of the MgB_2 lattice parameters parallel to the SPS pressing force (F_{SPS}, Fig. 2a), which generates an expansion of the unit cell in the perpendicular direction (macrostrain). This behavior is valid for both *a* and *c* constants of MgB_2 because, the samples are only partially textured, and the crystallites could have different orientations to the pressing force. The effect of compression and expansion is more directly transferred to the *a* and *c* lattice constants when the unit cells (crystallites) are oriented in the two extreme positions depicted in the inset of Fig. 3b. As the orientation degree increases, the probability that the unit cell is orientated with *c* parallel to the compression force increases, hence, the effect upon the values of *a* and *c* is higher. In the same key, one can comment on the decrease of the microstrain with the enhancement of texturing (Fig. 3c). Microstrain measures the dispersion of the interplanar spacings, which may originate from many sources, e.g., local lattice strain (caused, for instance, by point defects or dislocations), or structure changes near the crystallite or grain boundary, or different lattice strain in different crystallites. This last cause is probably preponderant for our partially textured and uni-axially-stressed bulk samples. The dispersion of the interplanar spacing decreases with orientation enhancement, and this is the case when measured both for S_{top} or S_{side} arrangements. In isotropic and macrostrain-free MgB_2 samples, the change in the *a*-lattice parameter of MgB_2 is considered an indicator of the degree of substitution of B by C [45–49]. Substitution of C for B leads to the creation of strain and

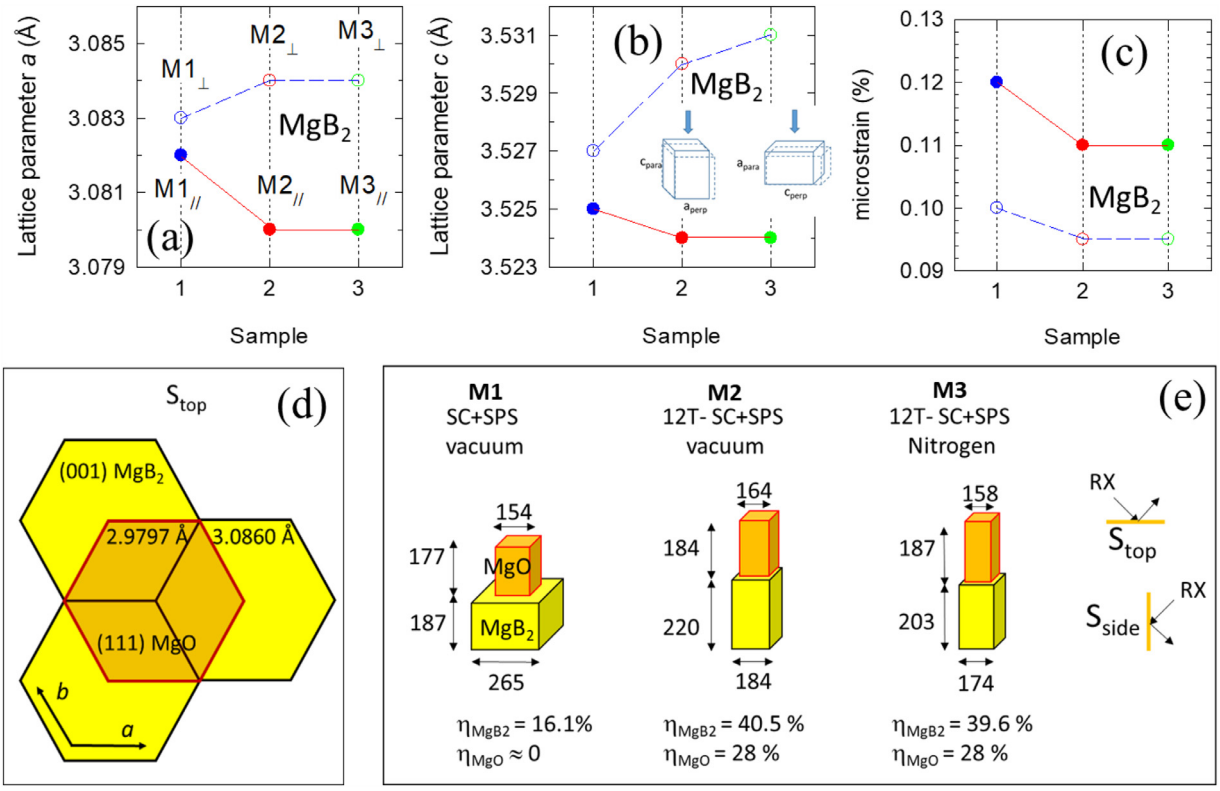

Fig. 3. Structural parameters for samples M1, M2, and M3 extracted from XRD data measured on S_{top} (//) and S_{side} (⊥), respectively: (a) lattice parameter *a* of MgB_2; (b) lattice parameter *c* of MgB_2. The inset in (b) explains intuitively the different values of the lattice constants obtained by XRD on the two perpendicular faces of the sample: the lattice shrinks in the SPS direction (//) and expands in the perpendicular directions (⊥). (c) Microstrain ε (%) of MgB_2; (d) Lattice matching relationship between (001) MgB_2 and (111) MgO. The distance between two neighboring Mg or B atoms in the (001) MgB_2 plane is 3.086 Å, while the distance between two oxygen or Mg atoms in the (111) MgO plane is 2.9797 Å The two crystal planes also have compatible rotational symmetry, namely of 6th order for (001) MgB_2 and 3rd order for (111) MgO; (e) comparison of MgB_2 and MgO crystallite sizes (in nanometers) of the textured samples.

distortion in the matrix because C–B bond is shorter than the B–B one. The dependence reported in the above-mentioned reports [45–49] works well for randomly oriented samples. In the case of highly *c*-axis oriented samples, the uniaxial pressure generated an enhancement of the anisotropic distribution of the strains and makes the model questionable. Therefore, additional investigations are required for a correct evaluation of the relationship between the doping level and lattice changes in highly textured MgB_2 samples. For our samples, it is reasonable to consider that some small amount of carbon intake, e.g., from the graphite die system occurs during SPS processing in the textured samples as in the randomly oriented ones [46].

Fig. 3e summarizes the average crystallite (coherence domain) sizes in vertical and lateral directions. One can notice that the MgO lateral size is always smaller than that of MgB_2, which could be an argument in favor of MgO epitaxy on MgB_2. The column-shaped MgB_2 crystallites are the constituents of the micron-size plate-shaped grains revealed in the SEM images presented below (Fig. 4).

When measured on S_{top} and S_{side}, the crystallite size of MgB_4 (83–98 nm, Table 1) shows differences and the tendencies for a certain measurement arrangement with the orientation degree are similar to those for MgB_2 although for this phase texturing was not found. Lack of correlations and explanations for the crystallite size dependencies have the origin in the complexity of the processes during processing, involving chemical reactions, solid, liquid, and gas phases, and also in the limitations in evaluation by Rietveld method of the crystallite size for the anisotropic crystals with a model that is suitable for spherical ones. A careful assessment and further studies are required.

The relative density of the samples is high, close to the theoretical value (Table 1). This is confirmed by the SEM images obtained on the highly oriented samples M2 and M3 (Fig. 4b and c2) showing few pores. Few closed pores are visible also in sample M1 (Fig. 4a) with a lower degree of orientation, but they can be the result of chemical etching. The plate-like hexagonal grains, which were ascribed to MgB_2 phase, are visible in the SEM images of highly oriented samples M2 and M3 (Fig. 4b, c1 and c2). The in-plane size of the platelets is about 1 μm. These micrographs confirm the *c*-axis texturing of MgB_2. We also note that samples with a higher level of orientation (e.g. M2, Fig. 4b) are more corrosion resistant than sample M1 (Fig. 4a). The anisotropic corrosion resistance is easy to understand from the crystal chemistry of MgB_2. The weak chemical bonding of Van der Waals type between the alternating Mg and B (*ab*)-planes favors a lower

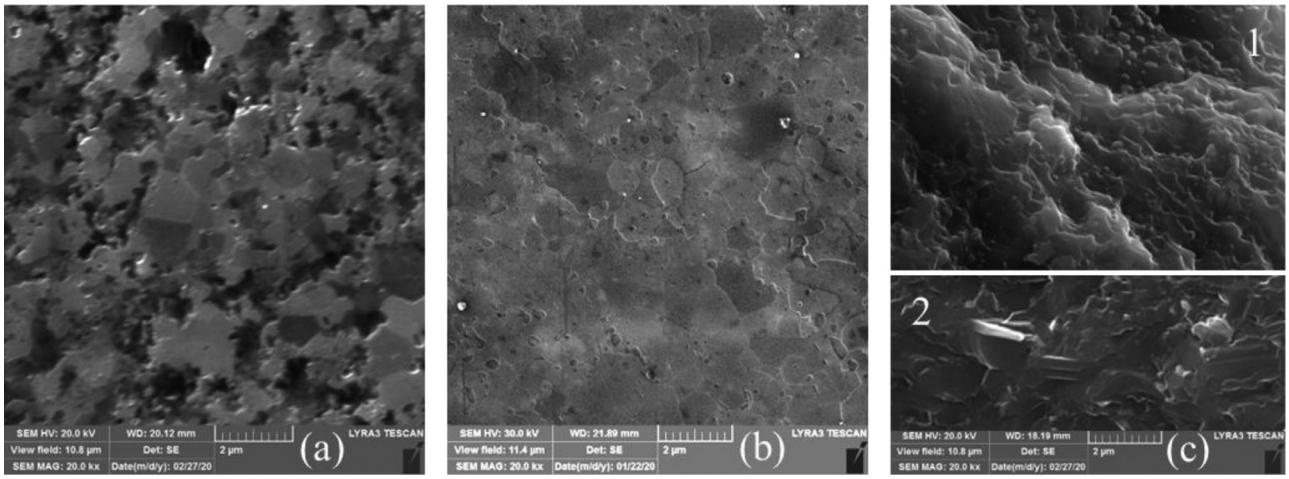

Fig. 4. SEM images taken on etched samples: (a) S_{top} of 0T-SC+SPS vacuum; (b) S_{top} of 12T-SC+SPS vacuum; (c) S_{side} of 12T-SC+SPS nitrogen (1 – fractured surface and 2 – polished surface).

corrosion resistance than in the plane where the bonds are strong.

The general TEM image on sample M3 shows grains with flat hexagonal surfaces (Fig. 5a). These grains (Fig. 5b) have the crystal structure of MgB_2 with the *c* axis perpendicular to the surface, as determined by selected area electron diffraction (SAED) (inset to Fig. 5b). Other grains with a bulky appearance are ascribed to MgO (Fig. 5c). Oxygen was also found at the grain boundaries, between MgB_2 grains (Fig. 5d). Distribution of MgO and MgB_2 grains can be also observed by using SAED mapping (Fig. 5g). By neglecting the MgO grains, the orientation map for MgB_2 is presented in Fig. 5h. The color and intensity code map from (Fig. 5f), which are based on the orientation map from Fig. 5h, indicates that most grains are (00l) textured (red color is dominant) but there are angular deviations from a perfect orientation. Indeed, the pole Fig. 5e for (00l) MgB_2 confirms that most grains of MgB_2 are *c*-axis oriented since the highest intensity is for the center of the pole figure. Horizontal *c*-axis orientation is also present (blue color, in Fig. 5f). Apparently, in the pole Fig. 5e there are present extra peaks with orientation at about 25–40° (from the vertical) that corresponds quite well to φ of about 39° determined by XRD. Nevertheless, this result might be just a statistical artefact since the number of measured grains is limited. The MgB_2 domain sizes of about 200 nm, highlighted in Fig. 5g, are close to the average lateral extent of the coherence domains of the MgB_2 resulted from XRD.

The EDS maps from Fig. 5i, and Fig. 5j show the distribution of elements. In some cases, nitrogen seems to accompany Mg and O from relatively large regions (Fig. 5j). There is also nitrogen in smaller nano areas not following the O distribution. As reported in Ref. [24], in randomly oriented samples fabricated by SPS in nitrogen, these nano grains were ascribed to phase MgB_9N. The amount and size of this phase are small and due to this it cannot be clearly observed in XRD patterns (Fig. 2b). In Ref. [24] the nano size of MgB_9N was determined to be comparable with the coherence length of MgB_2 (10–20 nm), and, thus, the precipitates of this phase can play the role of effective pinning centers. Confirmation of the presence of the MgB_9N phase in the samples from this work requires additional observations by electron microscopy.

3.2. Superconductivity aspects from magnetic measurements of the investigated samples

Fig. 6a shows magnetization curves with temperature. The critical temperatures T_c are $T_c = 37.5$ K, 38.4 K, and 38.3 K for the samples M1, M2, and M3, respectively. The slightly higher critical temperature of the samples M2 and M3 with a better texture is probably due to the slightly lower level of the microstrain [50] noticed in these samples (Fig. 3c).

The $J_c(H)$ curves at 5–35 K (see, e.g., curves for 5 and 20 K in Fig. 6b and Fig. 6c) of all samples are pushed to higher applied fields H when the measurement is performed in parallel geometry, i.e., $H \parallel H_0$, than when $H \perp H_0$ but converge to the same value at zero field. Nevertheless, a small anisotropy of zero-field critical current density J_{c0} ($J_{c0,\parallel} > J_{c0,\perp}$) at any investigated temperature can be visualized in Fig. 6d. Samples M2 and M3 with a higher level of orientation ($\eta = 40.5$ and 39.6%) have a higher difference between $J_{c\parallel}$ and $J_{c\perp}$ when compared with sample M1 ($\eta = 16.1\%$). At low temperatures (e.g., at 5 K, Fig. 6c), this difference is perhaps further expanded by the presence of nitrogen in sample M3. The influence of orientation can be understood based on the following observation. In a parallel field, the Lorentz force would try to move the vortices across the grain boundaries which provide a strong pinning. Hence, a high $J_{c\parallel}$ occurs. In the direction perpendicular to the surface, the MgB_2 platelets are defined as a high/dominant number of stacked interfaces parallel to the S_{top} surface. When the measuring field is applied in a perpendicular geometry, i.e. parallel to the (001) planes, the Lorentz force drives the vortices along the grain boundaries to positions that make the field gradient smaller and, consequently, the $J_{c\perp}$ is smaller than in the previous case. However, this scenario should take into account also other

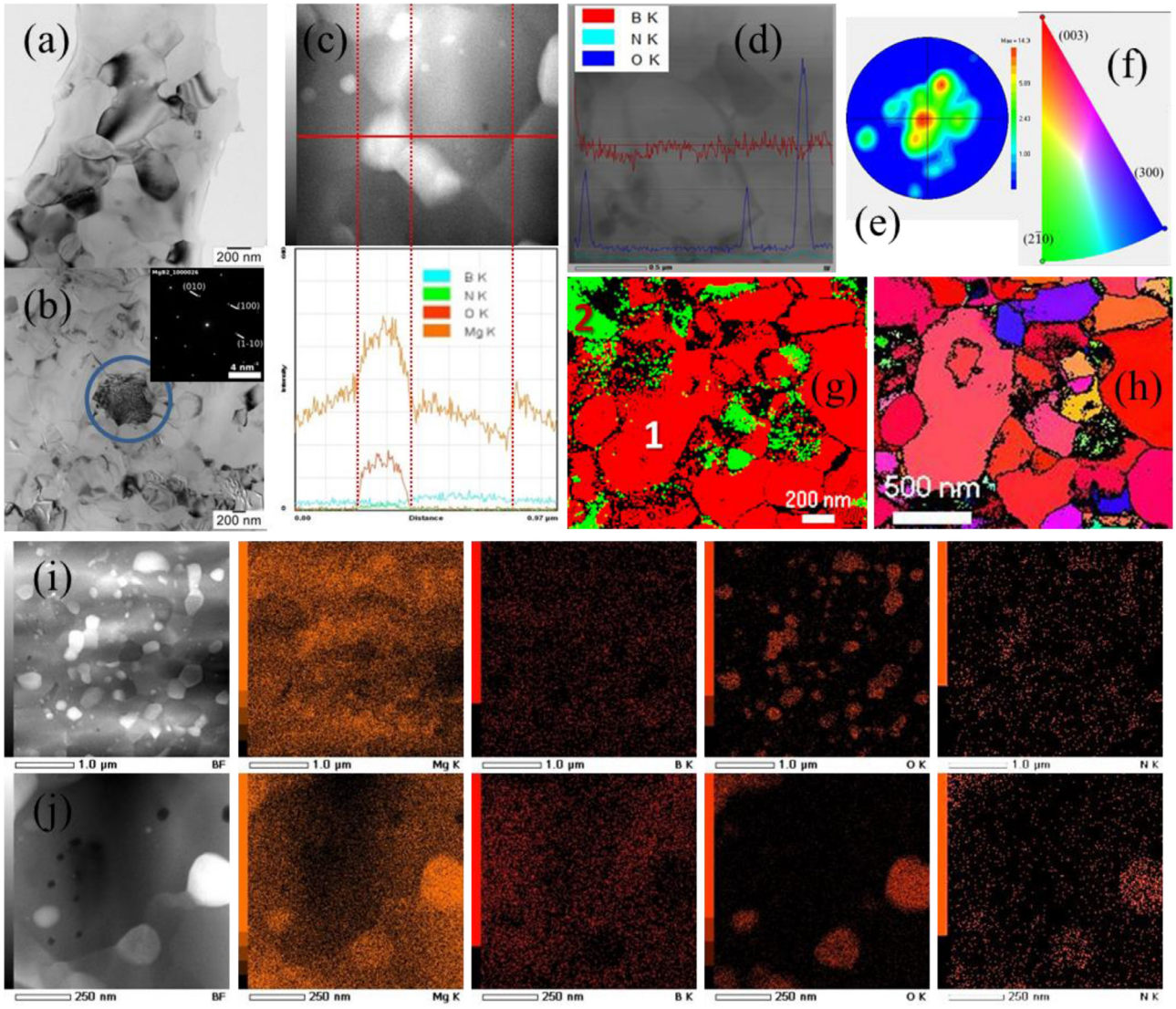

Fig. 5. TEM/EDS images on bulk sample 'M3': (a) general TEM image; (b) detail showing the hexagonal surface of a MgB_2 grain as identified by SAED (inset); (c) TEM image and line scan showing that white grains are MgO; (d) TEM image and EDS line scan showing grain boundaries containing oxygen; (g) SAED map that identifies the crystal structures of 1 – MgB_2 (red) and 2 – MgO (green); (h)= SAED map showing the degree of orientation of MgB_2 that corresponds to pole figure for (00l) from (e) and orientation color code from (f); (i) and (j) TEM images at two different magnifications and EDS maps for Mg, B, O, and N.

factors such as the inhomogeneity of the lattice parameters due to doping or stoichiometry variations, inhomogeneity and anisotropy of the microstrain due to orientation and to the presence of precipitates and defects. For example, in sample M3 introduction of nitrogen modifies the grain boundaries due to the occurrence of MgB_9N nano precipitates.

The indicated factors influence the coherence length size and pinning, thus, impacting superconducting parameters.

The temperature dependence of the irreversibility field (Fig. 6e) follows the law:

$$H_{irr} = H_{irr}(0)\left[1 - \left(\frac{T}{T_c}\right)^2\right]^{\beta}, \tag{6}$$

Both $H_{\mathrm{irr}}(0)$ and β are strongly dependent on the orientation (Table 2). The values of β are grouped around two different values within the error of measurement: when $H \parallel H_0$, the exponent is rather high $\beta_{\parallel} \geq 1.7$, whereas for $H \perp H_0$, $\beta_{\perp}$ has an average value $\bar{\beta}_{\perp} \approx 1.5$, which is close to the classical value of 1.5 [51,52]. For an increasing orientation degree η, $H_{\mathrm{irr},\parallel}(0)$ increases and $H_{\mathrm{irr},\perp}(0)$ decreases (Table 2, inset to Fig. 6e). It is noteworthy that the increase of $H_{\mathrm{irr}}(0)$ with orientation η for $H \parallel H_0$ ('$M1_{\parallel}$', '$M2_{\parallel}$', '$M3_{\parallel}$') is more pronounced than decrease for $H \perp H_0$ ('$M1_{\perp}$', '$M2_{\perp}$', '$M3_{\perp}$') (see inset to Fig. 6e). This result is important for practical applications and motivates the use of textured MgB_2 bulks. A linear fit of the η-dependence of the zero-temperature irreversibility $H_{\mathrm{irr}}(0)$ for $H \parallel H_0$ and $H \perp H_0$ provides close values for a random orientation ($\eta = 0$): $H_{irr,\parallel}|_{\eta=0} = 7.50 \pm 0.02$ and $H_{irr,\perp}|_{\eta=0} = 7.02 \pm 1.90$. A consequence of the existence of different irreversibility fields is the divergence of the current anisotropy, $\gamma_J = J_{c,\parallel}/J_{c,\perp}$ at $H_{\mathrm{irr},\perp}$. The depen-

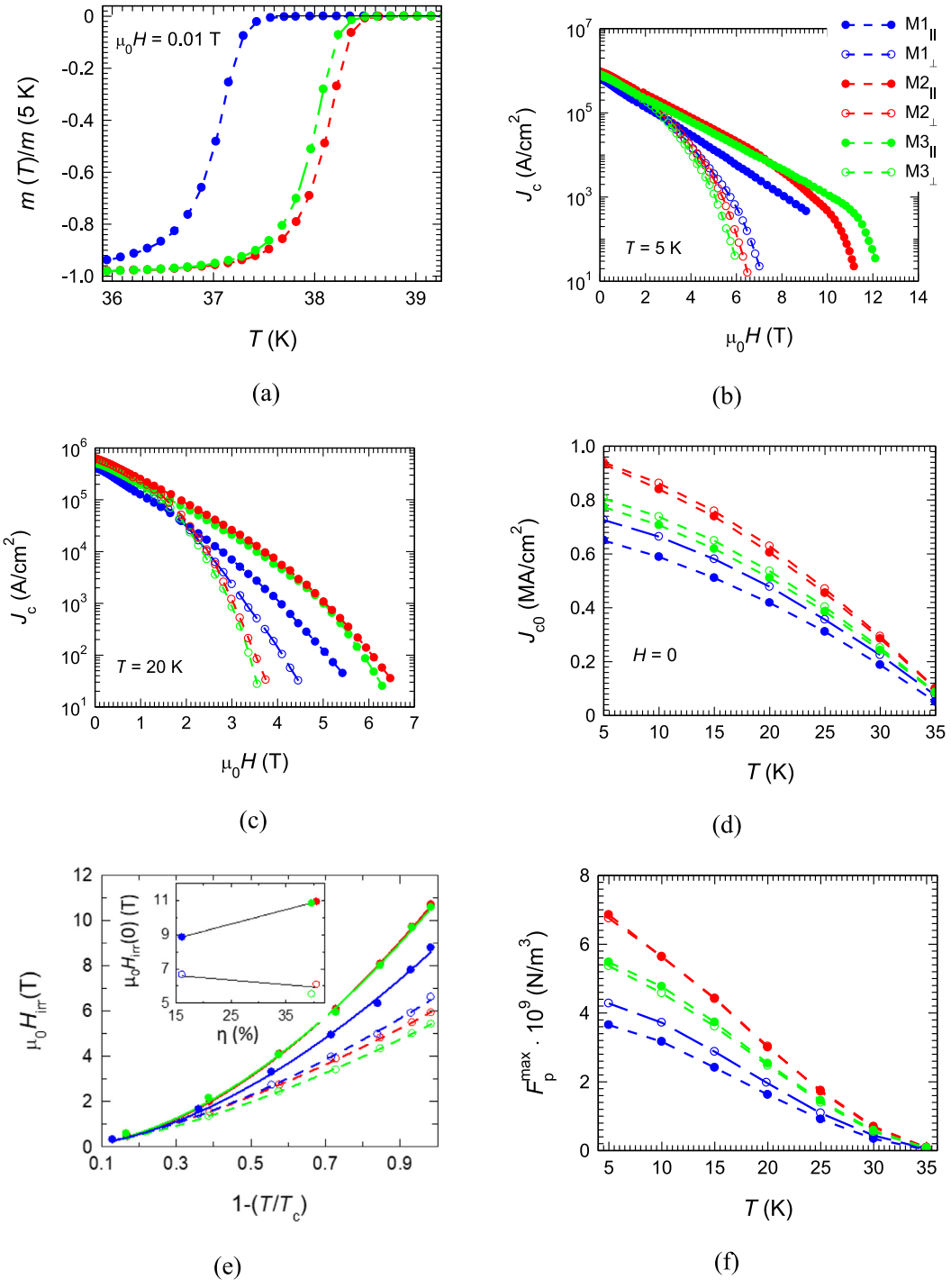

Fig. 6. (a) Reduced magnetization curves vs. temperature; (b) and (c) curves of critical current density $J_c(\mu_0 H)$ at 5 K and 20 K, respectively; (d) zero-field critical current density J_{c0} with temperature; (e) temperature dependence of the irreversibility field H_{irr} of MgB_2 samples in the parallel and perpendicular geometries of measurements. Lines are fits with Eq. (6). Inset shows the dependence of the irreversibility fields on the degree of (001) orientation η. The lines are linear fits. All the fit parameters are shown in the Table 2; (f) volume maximum pinning force with temperature.

Table 2.
Fit parameters with Eq. (6) of the irreversibility curves vs. temperature (Fig. 6e).

Sample	$\mu_0 H_{irr,\perp}(0)$ (T)	$\mu_0 H_{irr,\parallel}(0)$ (T)	$\beta_\perp$	$\beta_\parallel$	δ
M1	6.67 ± 0.07	8.87 ± 0.12	1.54 ± 0.04	1.71 ± 0.08	0.13 ± 0.01
M2	6.10 ± 0.02	10.99 ± 0.05	1.45 ± 0.01	1.82 ± 0.02	0.31 ± 0.02
M3	5.54 ± 0.03	10.85 ± 0.11	1.48 ± 0.02	1.70 ± 0.05	0.23 ± 0.02

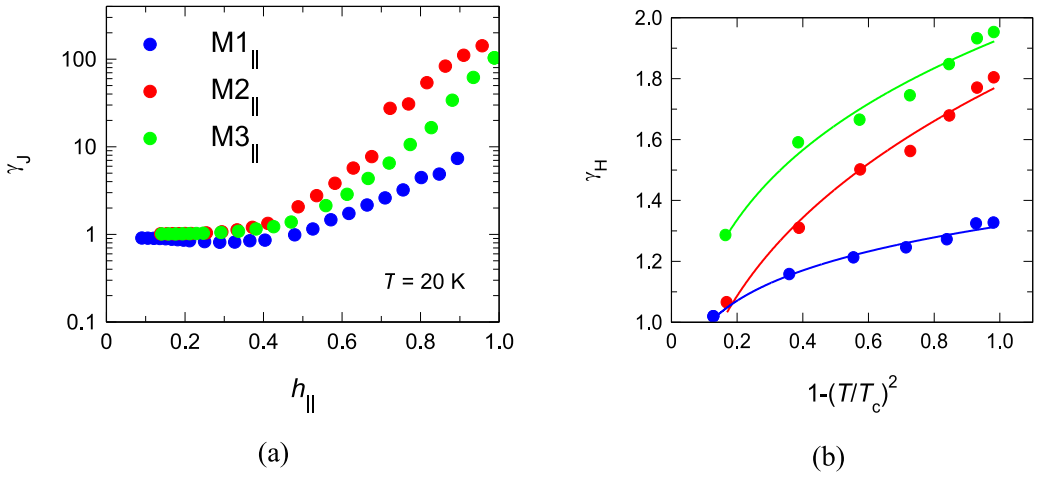

Fig. 7. (a) Current anisotropy γ_J as a function of the applied field relative to the irreversibility field for parallel direction $h_{\|} = H/H_{irr,\|}$ at 20 K; (b) temperature dependence of the anisotropy of the irreversibility field γ_H in samples M1$_{\|}$, M2$_{\|}$ and M3$_{\|}$. Continuous lines are fits with Eq. (7).

dence at 20 K of γ_J on the reduced field $h_{\|} = H/H_{irr,\|}$ for our samples is presented in Fig. 7a. A second consequence is that there is a temperature dependence of the anisotropy of the H_{irr}, $\gamma_H = H_{irr}^{||}/H_{irr}^{\perp}$ described by:

$$\gamma_H = \gamma_H(0)\left[1-(T/T_c)^2\right]^{\delta}, \quad (7)$$

with $\delta = \beta_{\|} - \beta_{\perp}$. The temperature dependence of γ_H is shown in Fig. 7b and the values of β are gathered in Table 2.

One observes that also the maximum pinning force $F_{p,\,max}$ is slightly larger in samples with a higher level of orientation (Fig. 6f).

Next, we present the results of the angular (α) dependence of superconducting parameters determined from magnetization loops $m(H)$ measured at 10 and 20 K. The weak angular dependence of J_{c0} (Fig. 8a) confirms the low field convergence of $J_{c\|}$ and $J_{c\perp}$ mentioned above. However, for sample M2, close to $\alpha = 90°$ the curve $J_{c0}(\alpha)$ is approximately constant, while for sample M3 there is a slow increase. The reason for this effect is missing. As expected, H_{irr} displays a high angular variation (Fig. 8b). The normalized pinning force $F_p^{max}/F_p^{max}(90°)$ displays a split of the main peak into two peaks positioned at $\alpha_{peak} = \pm$ 25–38° (Fig. 8c). The values of $|\alpha_{peak}| \leq \varphi$ (Table 1). They likely correspond also with results of the pole figure from TEM measurements (Fig. 5e, see also text in Section 3.1): in pole figures there is a main central peak accompanied by satellite peaks. The intensity of the two better resolved satellite peaks in the pole figure is not equal and this might be the reason for different intensities of the $F_p^{max}/F_p^{max}(90°)$ when α is positive or negative, but more research is needed. Overall, the peak of $F_p^{max}/F_p^{max}(90°)$ without considering its split is broad and this might be convenient for applications. Following this idea, the result may suggest that from a practical viewpoint, a partially textured but optimized (00l) MgB_2 material might be more valuable than a perfectly textured one. More research is needed to demonstrate this idea. Finally, we observe that the reduced field of the pinning force $h_0 = H(F_{p,\,max})/H_{irr}$ as a function of α has a minimum at $\alpha = 0°$ ($H \parallel H_0$). The minimum values of h_0 (Fig. 8d) are in the range 0.12–0.16 ($\alpha \sim 0°$). These values are smaller than the lowest theoretical value $h_0 = 0.2$ corresponding to the pinning on the grain boundaries [53] which remain the dominant pinning mechanism in MgB_2 [54]). As already introduced before, the favorable direction for superconductivity in (001) oriented MgB_2 is when $H \parallel H_0$ ($H \parallel c$-axis) and one can take advantage of a better connectivity and of an effective use of grain boundaries for pinning. To further observe this effect in terms of the pinning behavior for different T and H, we assessed as an example the pinning activation energy U^* from relaxation measurements for sample M3 and we compare the curves with those for a reference randomly oriented sample prepared by SPS without the slip casting step (Fig. 9).

The activation energy U^* increases with temperature in the collective (elastic) vortex-creep regime where the vortex phase is ordered [55] and decreases for plastic (dislocation mediated) creep where the vortex phase is disordered [56]. Curves for studied samples show this trend as one can observe in Fig. 9a. The crossover at about 9 K can be understood in terms of an energy balance relation, where the thermal energy can be neglected for strongly pinned samples when T is much lower than T_c. Therefore, at low T, the relaxation is smaller leading to a J closer to J_c, the effective pinning is weak and the inter-vortex interactions play an important role, giving rise to collective pinning. At high T the energy balance changes, because J relaxes faster and U^* increases. In these conditions, in the vortex system, dislocations occur due to vortex pinning and the creep becomes plastic. Roughly, this dynamic crossover appears when the effective depth of the pinning potential well equals the vortex deformation energy [57]. No crossover was observed in $U^*(H)$ and U^* decreases with increasing field, which is characteristic for plastic creep (Fig. 9b).

Curves $U^*(H)$ and $U^*(T)$ measured on the oriented sample M3 for the applied magnetic field in the parallel and perpendicular directions indicate on the anisotropy of U^*. The

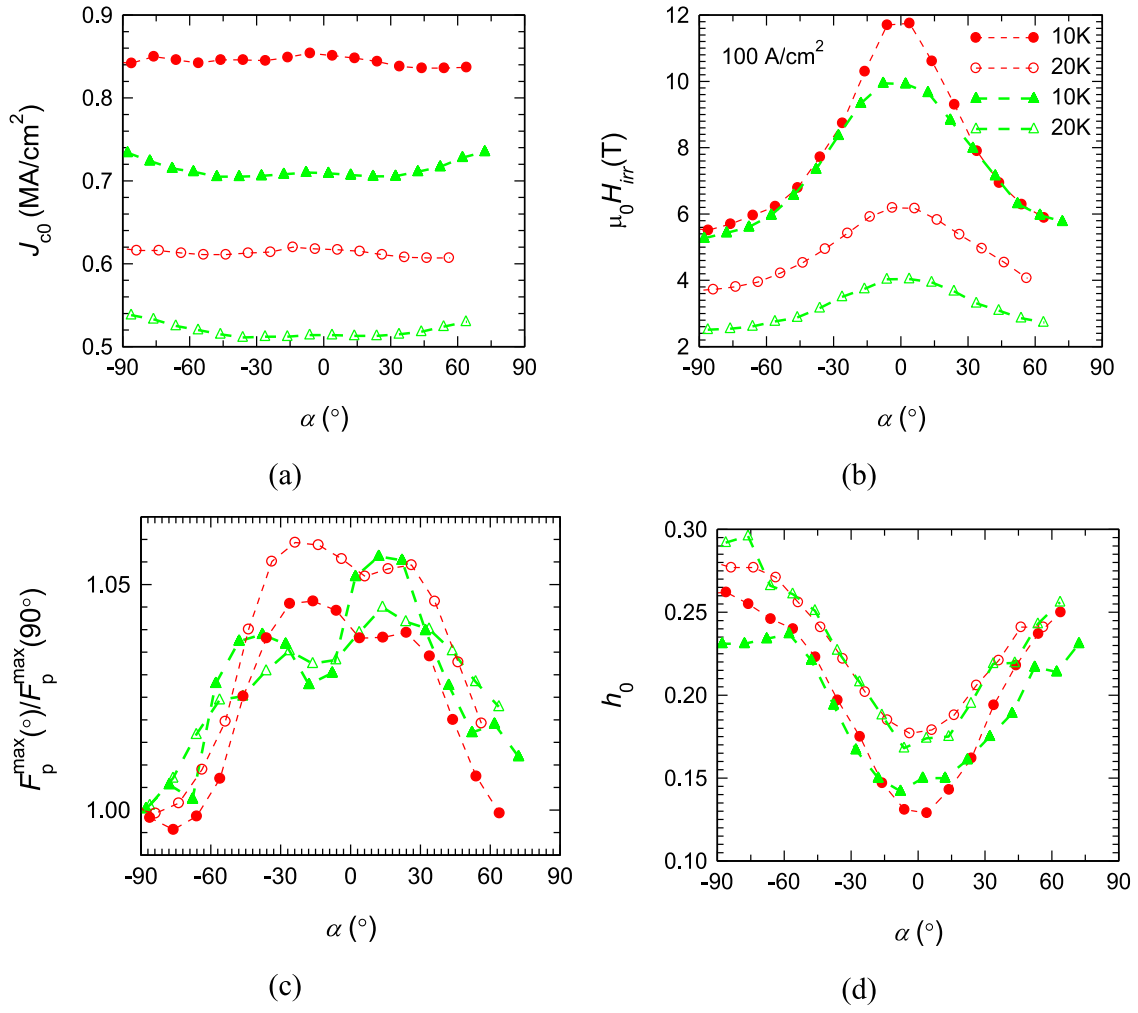

Fig. 8. Curves of: (a) zero-field critical current density J_{c0}; (b) irreversibility field $\mu_0 H_{irr}$; (c) normalized pinning force $F_p^{max}/F_p^{max}(90°)$; (d) h_0 as a function of applied field orientation angle α (0° denotes the $H \parallel H_0$ position) at 10 and 20 K for highly textured sample M2 in red and sample M3 in green.

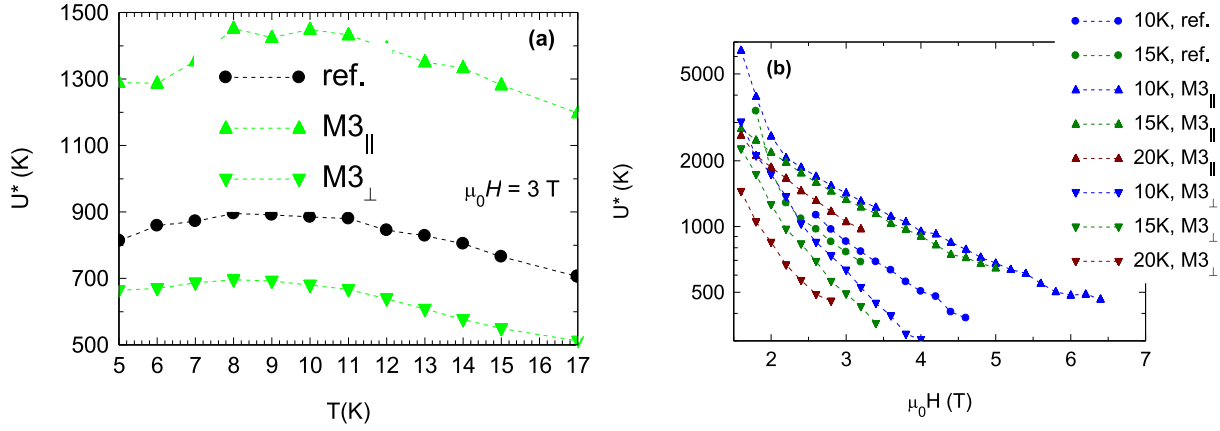

Fig. 9. The pinning activation energy as a function of temperature (for an applied magnetic field of 3 T) (a) and applied magnetic field (b). Sample denoted reference is a randomly oriented sample made from the same raw material and by SPS, but without slip casting.

pinning activation energy U^* of the sample M3 measured in parallel geometry ($H \parallel H_0$) is higher than for the reference sample, whereas the measurement in perpendicular geometry provides a lower U^*. Similar to the irreversibility field, this behavior is related to different density of barriers, namely to grain boundaries that a vortex encounters when its orientation is parallel to the plate or perpendicular on it. The values and curves shape of U^* are comparable with data reported in literature for pristine, added or proton irradiated MgB_2 bulks [58–61].

4. Conclusion

The approach from this work demonstrates new possibilities for further improvements of the MgB_2 superconductor and its processing technology.

We have shown that de-agglomeration and homogenization of the colloidal solution by high energy ultra-sonication during slip casting promotes (00l) orientation of the MgB_2 grains in the spark-plasma-sintered bulks. When during slip casting a magnetic field is not applied, the degree of orientation in the sintered sample attains ∼16%. The degree of orientation is further enhanced towards high values (∼40%), if during slip casting a high magnetic field of 12 T is applied. Some orientation was detected also for the grains of the secondary MgO phase.

Anisotropy of structural, microstructural and superconducting parameters of MgB_2 is analyzed and corroborated. The efficiency of grain boundaries on vortex pinning depends on orientation. The peak of $F_p^{max}/F_p^{max}(90°)$ was found to be broad in the highly oriented samples from this work suggesting that for practical applications a partially textured, but optimized (00l) MgB_2 bulk might be more suitable than a material with perfect 100% (00l) texture. This result and the pinning activation energy behavior provide the first elements necessary for design, fabrication and control of textured MgB_2 bulks (Eqs. (1)–(5)).

Declarations of Competing Interest

None.

Acknowledgments

Authors gratefully acknowledge financial support from MCI-UEFISCDI Romania, the projects PN030101 (21 N/2019), 5PTE/2020 – BIOTEHKER, and POC 37_697 no. 28/01.09.2016 REBMAT.

References

[1] J.C. Loudon, S. Yazdi, T. Kasama, N.D. Zhigadlo, J. Karpinski, Phys. Rev. B 91 (2015) 054505, doi:10.1103/PhysRevB.91.054505.
[2] S.X. Dou, W.K. Yeoh, J. Horvat, M. Ionescu, Appl. Phys. Lett. 83 (2003) 4996–4998, doi:10.1063/1.1634378.
[3] M.S.A. Hossain, J.H. Kim, X. Xu, X.L. Wang, M. Rindfleisch, M. Tomic, M.D. Sumption, E.W. Collings, S.X. Dou, Supercond. Sci. Technol. 20 (2007) L51, doi:10.1088/0953-2048/20/8/L03.
[4] D. Patel, M. Shahriar, A. Hossain, A. Motaman, S. Barua, M. Shahabuddin, J.H. Kim, Cryogenics 63 (2014) 160–165, doi:10.1016/j.cryogenics.2014.04.016.
[5] D. Rodrigues, L.B.S. da Silva, V.C.V. Metzner, E.E. Hellstrom, Phys. Procedia 36 (2012) 468–474, doi:10.1016/j.phpro.2012.06.219.
[6] D. Gajda, A. Morawski, A.J. Z.aleski, W. Haßler, K. Nenkov, M.A. Rindfleisch, E. Zuchowska, G. Gajda, T. Czujko, T. Cetner, M.S.A. Hossain, J. Appl. Phys. 117 (2015) 173908, doi:10.1063/1.4919364.
[7] M.S.A. Hossain, C. Senatore, M. Rindfleisch, R. Flukiger, Supercond. Sci. Technol. 24 (2011) 075013, doi:10.1088/0953-2048/24/7/075013.
[8] R. Flukiger, M.S.A. Hossain, C. Senatore, M. Rindfleisch, Phys. C 471 (2011) 1119–1123, doi:10.1016/j.physc.2011.05.139.
[9] G. Aldica, D. Batalu, S. Popa, I. Ivan, P. Nita, Y. Sakka, O. Vasylkiv, L. Miu, I. Pasuk, P. Badica, Phys. C 477 (2012) 43–50, doi:10.1016/j.physc.2012.01.023.
[10] J.G. Noudem, L. Dupont, P. Bernstein, Mater. Res. Soc. Symp. Proc. 1807 (2015) 7–10, doi:10.1557/opl.2015.675.
[11] J.G. Noudem, L. Dupont, L. Gozzelino, P. Bernstein, Mater. Today Proc. 3 (2016) 545–549, doi:10.1016/j.matpr.2016.01.088.
[12] J. Schmidt, W. Schnelle, Y. Grin, R. Kniep, Solid State Sci. 5 (2003) 535–539, doi:10.1016/S1293-2558(03)00026-8.
[13] S.Y. Lee, S.I. Yoo, Y.W. Kim, N.M. Hwang, D.Y. Kim, J. Am. Ceram. Soc. 86 (2003) 1800–1802, doi:10.1111/j.1151-2916.2003.tb03559.x.
[14] K.J. Song, C. Park, S.W. Kim, R.K. Ko, H.S. Ha, H.S. Kim, S.S. Oh, Y.K. Kwon, S.H. Moon, S.I. Yoo, Phys. C 426-431 (2005) 588–593, doi:10.1016/j.physc.2005.05.022.
[15] S.H. Shim, K.B. Shim, J.W. Yoon, J. Am. Ceram. Soc. 88 (2005) 858–861, doi:10.1111/j.1551-2916.2005.00220.x.
[16] H.L. Suo, Y. Wang, H.X. Ma, L. Ma, M. Liu, Y. Zhao, M.L. Zhou, Phys. C 460-462 (2007) 620–622, doi:10.1016/j.physc.2007.04.204.
[17] D.K. Kang, D.W. Kim, S.H. Choi, C.J. Kim, I.S. Ahn, Met. Mater. Int. 15 (2009) 15–19, doi:10.1007/s12540-009-0015-x.
[18] D.K. Kang, D.W. Kim, C.J. Kim, I.S. Ahn, J. Nanosci. Nanotechnol. 10 (2010) 142–146, doi:10.1166/jnn.2010.1501.
[19] A. Murakami, J. Noudem, Z. Guesmi, T. Kudo, A. Iwamoto, Phys. Procedia 65 (2015) 77–80, doi:10.1016/j.phpro.2015.05.128.
[20] C. Wang, Y. Ma, X. Zhang, D. Wang, Z. Gao, C. Yao, C. Wang, H. Oguro, S. Awaji, K. Watanabe, Supercond. Sci. Technol. 25 (2012) 035018, doi:10.1088/0953-2048/25/3/035018.
[21] M.A. Grigoroscuta, V. Sandu, A. Kuncser, I. Pasuk, G. Aldica, T. Suzuki, O. Vasylkiv, P. Badica, Supercond. Sci. Technol. 32 (2019) 125001, doi:10.1088/1361-6668/ab4620.
[22] L. Gozzelino, B. Minetti, R. Gerbaldo, G. Ghigo, F. Laviano, G. Lopardo, C. Plapcianu, A. Agostino, S. Cagliero, M. Truccato, L. Zilberti, E. Mezzetti, J. Supercond. Nov. Magn. 24 (2010) 307–312, doi:10.1007/s10948-010-0993-4.
[23] C. Plapcianu, A. Agostino, P. Badica, G.V. Aldica, E. Bonometti, G. Ieluzzi, S. Popa, M. Truccato, S. Cagliero, Y. Sakka, O. Vasylkiv, R. Vidu, Ind. Eng. Chem. Res. 51 (2012) 11005–11010, doi:10.1021/ie3005429.
[24] P. Badica, M. Burdusel, S. Popa, I. Pasuk, I. Ivan, H. Borodianska, O. Vasylkiv, A. Kuncser, A.M. Ionescu, L. Miu, G. Aldica, Supercond. Sci. Technol. 29 (2016) 105020, doi:10.1088/0953-2048/29/10/105020.
[25] M. Grigoroscuta, G. Aldica, I. Pasuk, M. Burdusel, V. Sandu, A. Kuncser, T. Suzuki, O. Vasylkiv, P. Badica, Mater. Res. Bull. 134 (2021) 111103, doi:10.1016/j.materresbull.2020.111103.
[26] M. Eisterer, W. Häßler, P. Kováč, Phys. Rev. B 80 (2009) 174516, doi:10.1103/PhysRevB.80.174516.
[27] W. Haßler, P. Kovac, M. Eisterer, A.B. Abrahamsen, M. Herrmann, C. Rodig, K. Nenkov, B. Holzapfel, T. Melisek, M. Kulich, M.V. Zimmermann, J. Bednarcik, J.C. Grivel, Supercond. Sci. Technol. 23 (2010) 065011, doi:10.1088/0953-2048/23/6/065011.
[28] Y. Sakka, T.S. Suzuki, J. Ceram. Soc. Jpn. 113 (2005) 26–36, doi:10.2109/jcersj.113.26.
[29] Y. Sakka, KONA Powder Part. J. 36 (2019) 114–128, doi:10.14356/kona.2019007.
[30] O. Vasylkiv, Y. Sakka, J. Am. Ceram. Soc. 84 (2001) 2489–2494, doi:10.1111/j.1151-2916.2001.tb01041.x.
[31] L. Lutterotti, Nucl. Inst. Methods Phys. Res. B 268 (2010) 334–340, doi:10.1016/j.nimb.2009.09.053.
[32] W.A. Dollase, J. Appl. Cryst. 19 (1986) 267–272, doi:10.1107/S0021889886089458.
[33] E. Zolotoyabko, J. Appl. Cryst. 42 (2009) 513–518, doi:10.1107/S0021889809013727.
[34] F.K. Lotgering, J. Inorg. Nucl. Chem. 9 (1959) 113–123, doi:10.1016/0022-1902(59)80070-1.
[35] G.W. Marks, L.A. Monson, Ind. Eng. Chem. 47 (1955) 1611–1620, doi:10.1021/ie50548a044.
[36] C.P. Bean, Phys. Rev. Lett. 8 (1962) 250–253, doi:10.1103/PhysRevLett.8.250.

[37] L. Miu, G. Aldica, P. Badica, I. Ivan, D. Miu, G. Jakob, Supercond. Sci. Technol. 23 (2010) 095002, doi:10.1088/0953-2048/23/9/095002.
[38] Y. Yeshurun, A.P. Malozemoff, A. Shaulov, Rev. Mod. Phys. 68 (1996) 911–949, doi:10.1103/RevModPhys.68.911.
[39] L. Miu, I. Ivan, G. Aldica, P. Badica, J.R. Groza, D. Miu, G. Jakob, H. Adrian, Phys. C 468 (2008) 2279–2282, doi:10.1016/j.physc.2008.08.001.
[40] P. Kovac, I. Husek, T. Melisek, J.C. Grivel, W. Pachla, V. Strbık, R. Diduszko, J. Homeyer, N.H. Andersen, Supercond. Sci. Technol. 17 (2004) L41–L46, doi:10.1088/0953-2048/17/10/L03.
[41] M. Miryala, S.S. Arvapalli, P. Diko, M. Jirsa, M. Murakami, Adv. Eng. Mater. 22 (2020) 1900750, doi:10.1002/adem.201900750.
[42] P. Badica, N.D. Batalu, M.C. Chifiriuc, M. Burdusel, M.A. Grigoroscuta, G. Aldica, I. Pasuk, A. Kuncser, M. Enculescu, M. Popa, L.G. Marutescu, I. Gheorghe, O. Thamer, C. Bleotu, G. Gradisteanu Pircalabioru, L. Operti, V. Bonino, A. Agostino, M. Truccato, J. Mater. Res. Technol. 12 (2021) 2168–2184, doi:10.1016/j.jmrt.2021.04.003.
[43] K. Kendall, Powder Technol. 58 (1989) 151–161, doi:10.1016/0032-5910(89)80109-3.
[44] A.J.M. van Erven, T.H. Kim, M. Muenzenberg, J.S. Moodera, Appl. Phys. Lett. 81 (2002) 4982, doi:10.1063/1.1530732.
[45] A.G. Bhagurkar, A. Yamamoto, L. Wang, M. Xia, A.R. Dennis, J.H. Durrell, T.A. Aljohani, N.H. Babu, D.A. Cardwell, Sci. Rep. 8 (2018) 13320, doi:10.1038/s41598-018-31416-3.
[46] G. Aldica, S. Popa, M. Enculescu, I. Pasuk, A.M. Ionescu, P. Badica, J. Supercond. Nov. Magn. 31 (2018) 317–325, doi:10.1007/s10948-017-4236-9.
[47] M. Avdeev, J.D. Jorgensen, R.A. Ribeiro, S.L. Bud'ko, P.C. Canfield, Phys. C 387 (2003) 301–306, doi:10.1016/S0921-4534(03)00722-6.
[48] S. Lee, T. Masui, A. Yamamoto, H. Uchiyama, S. Tajima, Phys. C 412–414 (2004) 31–35, doi:10.1016/j.physc.2004.01.036.
[49] S.X. Dou, O. Shcherbakova, W.K. Yoeh, J.H. Kim, S. Soltanian, X.L. Wang, C. Senatore, R. Flukiger, M. Dhalle, O. Husnjak, E. Babic, Phys. Rev. Lett. 98 (2007) 097002, doi:10.1103/PhysRevLett.98.097002.
[50] X.Z. Liao, A. Serquis, Y.T. Zhu, D.E. Peterson, M. Mueller, H.F. Xu, Supercond. Sci. Technol. 17 (2004) 1026, doi:10.1088/0953-2048/17/8/014.
[51] K.A. Muller, M. Takashige, J.G. Bednorz, Phys. Rev. Lett. 58 (1987) 1143, doi:10.1103/PhysRevLett.58.1143.
[52] Y. Yeshurun, A.P. Malosemoff, Phys. Rev. Lett. 60 (1988) 2202, doi:10.1103/PhysRevLett.60.2202.
[53] D. Dew-Hughes, Philos. Mag. A J. Theor. Exp. Appl. Phys. 3 (1974) 293, doi:10.1080/14786439808206556.
[54] D.C. Larbalestier, L.D. Cooley, M.O. Rikel, A.A. Polyanskii, J. Jiang, S. Patnaik, X.Y. Cai, D.M. Feldmann, A. Gurevich, A.A. Squitieri, M.T. Naus, C.B. Eom, E.E. Hellstrom, R.J. Cava, K.A. Regan, N. Rogado, M.A. Hayward, T. He, J.S. Slusky, P. Khalifah, K. Inumaru, M. Haas, Nature 410 (2001) 186–189, doi:10.1038/35065559.
[55] M.V. Feigel'man, V.B. Geshkenbein, A.I. Larkin, V.M. Vinokur, Phys. Rev. Lett. 63 (1989) 2303–2306, doi:10.1103/PhysRevLett.63.2303.
[56] Y. Abulafia, A. Shaulov, Y. Wolfus, R. Prozorov, L. Burlachkov, Y. Yeshurun, D. Majer, E. Zeldov, H. Wühl, V.B. Geshkenbein, V.M. Vinokur, Phys. Rev. Lett. 77 (1996) 1596–1599, doi:10.1103/PhysRevLett.77.1596.
[57] G. Blatter, M.V. Feigel'man, V.B. Geshkenbein, A.I. Larkin, V.M. Vinokur, Rev. Mod. Phys. 66 (1994) 1125–1388, doi:10.1103/RevModPhys.66.1125.
[58] G. Pasquini, A. Serquis, A.J. Moreno, G. Serrano, L. Civale, J. Appl. Phys. 114 (2013) 023907, doi:10.1063/1.4813132.
[59] M. Reissner, S. Sorta, L. Bulla, T. Melišek, P. Kováč, J. Supercond. Nov. Magn. 26 (2013) 1543–1546, doi:10.1007/s10948-012-2018-y.
[60] P. Badica, G. Aldica, M. Burdusel, S. Popa, R.F. Negrea, M. Enculescu, I. Pasuk, L. Miu, Supercond. Sci. Technol. 27 (2014) 095013, doi:10.1088/0953-2048/27/9/095013.
[61] V. Sandu, L. Craciun, A.M. Ionescu, G. Aldica, L. Miu, A. Kuncser, Phys. C 528 (2016) 27–34, doi:10.1016/j.physc.2016.07.006.